NASA Technical Memorandum 87128

Development of an Explicit Multigrid Algorithm for Quasi-Three-Dimensional Viscous Flows in Turbomachinery

Rodrick V. Chima
Lewis Research Center
Cleveland, Ohio

Prepared for the
Twenty-fourth Aerospace Sciences Meeting
sponsored by American Institute of Aeronautics and Astronautics
Reno, Nevada, January 6–9, 1986

NASA

DEVELOPMENT OF AN EXPLICIT MULTIGRID ALGORITHM FOR QUASI-THREE-DIMENSIONAL VISCOUS FLOWS IN TURBOMACHINERY

Rodrick V. Chima
National Aeronautics and Space Administration
Lewis Research Center
Cleveland, Ohio 44135

Abstract

A rapid quasi-three-dimensional analysis has been developed for blade-to-blade flows in turbomachinery. The analysis solves the unsteady Euler or thin-layer Navier-Stokes equations in a body-fitted coordinate system. It accounts for the effects of rotation, radius change, and stream-surface thickness. The Baldwin-Lomax eddy-viscosity model is used for turbulent flows. The equations are solved using a two-stage Runge-Kutta scheme made efficient by use of vectorization, a variable time-step, and a flux-based multigrid scheme, which are all described. A stability analysis is presented for the two-stage scheme. Results for a flat-plate model problem show the applicability of the method to axial, radial, and rotating geometries. Results for a centrifugal impeller and a radial diffuser show that the quasi-three-dimensional viscous analysis can be a practical design tool.

Introduction

Turbomachinery intended to produce large amounts of power from a small volume often require use of radial-flow or mixed-flow components, that is, components in which the streamwise velocity is not strictly axial. Radial-flow turbomachines such as centrifugal impellers, radial diffusers, and radial-inflow turbines have a predominantly radial flow direction. Mixed-flow turbomachines may be used when restrictions on space prevent a completely radial flow. Complicated geometries, shock waves, and viscous phenomena make analysis of radial- or mixed-flow turbomachines more difficult than analysis of strictly axial-flow machines.

Analysis of axial-flow turbomachinery blade rows is usually simplified by modelling a blade section as a flat cascade. The governing equations for a flat cascade are the same two-dimensional flow equations that are solved for isolated airfoils, so cascade analyses often draw heavily on numerical techniques developed for two-dimensional external flows. Examples of flat cascade analyses include panel methods,[1] potential methods,[2] Euler solutions,[3,4] and Navier-Stokes solutions.[5,6]

Flows in radial- or mixed-flow turbomachines are inherently three-dimensional, requiring specification of the axial, radial, and tangential velocity components to fully specify the flow. A simplification that allows these machines to be analyzed in two dimensions was proposed by C.H. Wu in 1952.[7] In Wu's model the flow is assumed to follow an axisymmetric stream surface (Wu's "S2 surface," Fig. 1). The radius and thickness of the stream surface are assumed to be known as functions of the streamwise distance. These quantities are usually obtained from an axisymmetric through-flow or "meridional" analysis,[8] sometimes coupled with a boundary layer analysis[9] on the hub and shroud.

The equations governing the flow along the stream surface combine the axial- and radial-velocity components into one streamwise component, and are thus two-dimensional. The solution can be resolved into three velocity components since the shape of the surface is known. Specifying the stream-surface thickness allows variable blade heights and end wall displacement thicknesses to be modelled. This is similar to specifying area change in the one-dimensional nozzle equations. Since the effects of radius change and stream-surface thickness are modelled in this analysis, it is termed "quasi-three-dimensional." Examples of quasi-three-dimensional turbomachinery analyses include panel methods,[10] stream-function methods,[11] potential methods,[12] and Euler methods.[13]

In the present work, the Euler and Navier-Stokes code developed for flat cascades in Ref. 6 has been extended to a quasi-three-dimensional analysis. It is thought that this is the first Navier-Stokes analysis to include the effects of rotation, radius change, and stream-surface thickness. The explicit MacCormack algorithm[14] used in[6] has been replaced with an explicit two-stage Runge-Kutta finite-difference algorithm based on the work of Jameson.[15] Efficiency is achieved by three means: vectorization, use of a variable time-step, and by use of a multigrid scheme developed by Ni[16] and modified by Johnson and Chima.[17-19]

Governing Equations

The axisymmetric (m,θ) coordinate system used for the quasi-three-dimensional analysis is shown in Fig. 1. Here the m-coordinate is defined by

$$dm^2 = dz^2 + dr^2 \tag{1}$$

and the θ-coordinate is defined by:

$$\theta = \theta' - \Omega t \tag{2}$$

where θ' is fixed in space and θ rotates with the blade row with angular velocity Ω. The radius r and the stream surface thickness h are taken to be known functions of m. In this coordinate system the dimensionless Navier-Stokes equations may be written in the following nearly-conservative form:

$$\partial_t q + \partial_m(F - Re^{-1}R) + \partial_\theta(G - Re^{-1}S) = K \tag{3}$$

where

$$q = rh\begin{bmatrix}\rho\\ \rho v_m\\ \rho v_\theta r\\ e\end{bmatrix} \qquad F = rh\begin{bmatrix}\rho v_m\\ \rho v_m^2 + p\\ (\rho v_m v_\theta)r\\ v_m(e+p)\end{bmatrix}$$

$$G = h\begin{bmatrix}\rho w_\theta\\ \rho v_m w_\theta\\ (\rho v_\theta w_\theta + p)r\\ w_\theta(e+p) + r\Omega p\end{bmatrix} \qquad K = rh\begin{bmatrix}0\\ K_2\\ 0\\ 0\end{bmatrix}$$

$$R = rh\begin{bmatrix}0\\ \sigma_{11}\\ \sigma_{12}r\\ R_4\end{bmatrix} \qquad S = h\begin{bmatrix}0\\ \sigma_{12}\\ \sigma_{22}r\\ S_4\end{bmatrix} \qquad (4)$$

and

$w_\theta = v_\theta - r\Omega$ is the relative tangential velocity component,

$e = \rho[C_v T + 1/2(v_m^2 + v_\theta^2)]$ is the total energy per unit volume,

$p = (\gamma - 1)[e - 1/2\rho(v_m^2 + v_\theta^2)]$ is the pressure,

$K_2 = (\rho v_\theta^2 + p - \sigma_{22})r_m/r + (p - \sigma_{33})h_m/h$

$r_m/r = \frac{1}{r}\frac{dr}{dm}$

$h_m/h = \frac{1}{h}\frac{dh}{dm}$

The viscous terms in the energy equation are:

$$R_4 = \frac{k}{(\gamma-1)Pr}\left(\partial_m a^2\right) + v_m\sigma_{11} + v_\theta\sigma_{12}$$

$$S_4 = \frac{k}{(\gamma-1)Pr}\left(1/r\partial_\theta a^2\right) + v_m\sigma_{12} + v_\theta\sigma_{22} \qquad (5)$$

where

$a = \sqrt{\gamma p/\rho}$ is the sonic velocity, and the normalized thermal conductivity k equals one.

The shear stress terms are:

$$\sigma_{11} = 2\mu\partial_m v_m + \lambda\nabla\cdot\bar{V}$$

$$\sigma_{22} = 2\mu(\partial_\theta v_\theta + v_m r_m)/r + \lambda\nabla\cdot\bar{V}$$

$$\sigma_{33} = 2\mu v_m h_m/h + \lambda\nabla\cdot\bar{V}$$

$$\sigma_{12} = \mu\left(\partial_m v_\theta - v_\theta r_m/r + 1/r\partial_\theta v_m\right)$$

and

$$\lambda\nabla\cdot\bar{V} = \frac{-2}{3}\mu\left[\partial_m v_m + v_m\left(r_m/r + h_m/h\right) + 1/r\partial_\theta v_\theta\right] \qquad (6)$$

is the dilitation.

The equations are nondimensionalized by arbitrary reference quantities (here the inlet total density and critical sonic velocity define the reference state), and the Reynolds number Re and the Prandtl number Pr must be specified in terms of that state. These equations assume that the specific heats C_p and C_v and the Prandtl number are constant, that Stokes' hypothesis $\lambda = -2/3\,\mu$ is valid, and that the effective viscosity may be written as

$$\mu = \mu_{laminar} + \mu_{turbulent}$$

Equations (3) to (6) are transformed from the (m,θ) coordinate system to a general body-fitted (ξ,η) coordinate system using standard methods. The thin-layer assumption is then used to eliminate viscous derivitives in the streamwise (ξ) direction, thereby reducing computational overhead while retaining the capability of computing separated flows. The resulting equations are similar to those developed by Katsanis.[20]

$$\partial_t\hat{q} + \partial_\xi\hat{F} + \partial_\eta(\hat{G} - Re^{-1}\hat{S}) = \hat{K} \qquad (7)$$

where

$$\hat{q} = \bar{J}^{-1}\begin{bmatrix}\rho\\ \rho v_m\\ \rho v_\theta r\\ e\end{bmatrix} \qquad \hat{F} = \bar{J}^{-1}\begin{bmatrix}\rho W^\xi\\ \rho v_m W^\xi + \xi_m p\\ (\rho v_\theta W^\xi + \bar{\xi}_\theta p)r\\ (e+p)W^\xi + \bar{\xi}_\theta r\Omega p\end{bmatrix}$$

$$\hat{K} = \bar{J}^{-1}\begin{bmatrix}0\\ K_2\\ 0\\ 0\end{bmatrix} \qquad \hat{G} = \bar{J}^{-1}\begin{bmatrix}\rho W^\eta\\ \rho v_m W^\eta + \eta_m p\\ (\rho v_\theta W^\eta + \bar{\eta}_\theta p)r\\ (e+p)W^\eta + \bar{\eta}_\theta r\Omega p\end{bmatrix}$$

$$\hat{S} = \bar{J}^{-1}\begin{bmatrix}0\\ \eta_m\sigma_{11} + \bar{\eta}_\theta\sigma_{12}\\ (\eta_m\sigma_{12} + \bar{\eta}_\theta\sigma_{22})r\\ S_4\end{bmatrix} \qquad (8)$$

and

$$K_2 = \left(\rho v_\theta^2 + p - Re^{-1}\sigma_{22}\right) r_m/r + (p - Re^{-1}\sigma_{33})\, h_m/h$$

$$S_4 = \frac{k}{(\gamma - 1)Pr}\left(\eta_m^2 + \bar{\eta}_\theta^2\right)\partial_\eta a^2 + v_m S_2 + v_\theta S_3$$

In Eq. (8) the overbars denote a rescaling of the metric terms:

$$\bar{\xi}_\theta = \xi_\theta / r; \qquad \bar{\eta}_\theta = \eta_\theta / r; \qquad \bar{J}^{-1} = rhJ^{-1} \tag{9}$$

where J is the Jacobian of the transformation

$$J = \xi_m \eta_\theta - \eta_m \xi_\theta = \frac{1}{(m_\xi \theta_\eta - m_\eta \theta_\xi)} \tag{10}$$

and the metric quantities are determined from the grid-point coordinates using central differences and:

$$\begin{aligned} \xi_m &= J\theta_\eta; \qquad \xi_\theta = -Jm_\eta; \\ \eta_m &= -J\theta_\xi; \qquad \eta_\theta = Jm_\xi \end{aligned} \tag{11}$$

The relative contravariant velocity components W^ξ and W^η along the ξ and η grid lines are given by:

$$W^\xi = \xi_m v_m + \bar{\xi}_\theta w_\theta; \qquad W^\eta = \eta_m v_m + \bar{\eta}_\theta w_\theta \tag{12}$$

The shear stress terms are found from Eq. (6) by replacing ∂_m with $\eta_m \partial_\eta$ and $1/r\partial_\theta$ with $\bar{\eta}_\theta \partial_\eta$.

The quasi-three-dimensional equations (Eqs. (7) to (12)) are similar to the two-dimensional equations solved in Ref. 6 except for the source term K_2, the radius appearing in the θ-momentum equation, the rescaled metrics (Eq. (9)), and the relative velocity component w_θ appearing in the contravariant velocities (Eq. (12)). Equations (7) to (12) reduce to the two-dimensional equations for constant r and h, and zero rotation. Note that Eqs. (7) to (12) are independent of the magnitude of the stream surface thickness h so that any function $h(m) > 0$ may be used. The equations do depend on the magnitude of the radius r because of the $1/r$ terms scaling ξ_θ and η_θ in Eq. (9).

For turbulent flows the two-layer eddy-viscosity model developed by Baldwin and Lomax[21] is used. In the (m,θ) coordinate system the wall shear τ_w and vorticity ω required by the model are given by

$$\tau_w = \sigma_{12\,w} = \mu\left(\partial_m v_\theta + 1/r\partial_\theta v_m - v_\theta r_m/r\right)_w \tag{13}$$

$$\omega = \frac{1}{2}\left(\partial_m v_\theta - 1/r\partial_\theta v_m + v_\theta r_m/r\right) \tag{14}$$

Computational Grid

Body-fitted grids for this work were generated using the GRAPE code (GRids about Airfoils using Poisson's Equation) developed by Sorenson.[22,23] Briefly, the code allows arbitrary specification of inner and outer boundary points, then generates interior points as a solution to a Poisson equation. Forcing terms in the Poisson equation are chosen such that desired grid spacing and intersection angles may be maintained at the inner and outer boundaries.

New inner and outer boundary subroutines were written for turbomachine geometries. The new inner boundary has constant spacing around blade leading and trailing edges, larger constant spacing over blade surfaces, and exponential stretching connecting the regions. The new outer boundary is composed of the mean-camber line between the blades, a quadratic extension upstream, and a linear extension downstream. The C-shaped grids are periodic over the pitch of the blade. Grids are generated in a Cartesian $(m,\bar{r}\theta)$ coordinate system, where $\bar{r}$ is some mean radius. The local radius and stream surface thickness are supplied to the Navier-Stokes code at a later time as tabulated functions of m, then spline-fit on to the grid. The terms r_m/r and h_m/h in Eqs. (7) and (8) are calculated using central differences and are stored.

Initial Conditions

Since a centrifugal compressor can produce pressure ratios of 5:1 or greater it is not generally possible to start a quasi-three-dimensional calculation with constant initial conditions. Instead an analytic solution of the one-dimensional flow equations with area change is used. Turbomachinery blades are usually designed based on desired leading- and trailing-edge velocity triangles, so the relative flow velocity W and angle α at the leading edge and the relative flow angle at the trailing edge are used as input for the initial conditions.

Using $()'$ to denote absolute total conditions and $()''$ to denote relative total conditions, the continuity and energy equations are

$$\dot{m} = \rho rh\Delta\theta W \cos\alpha = \text{constant} \tag{15}$$

$$I = C_p T' - r\Omega v_\theta = C_p T'' - 1/2\, r^2\Omega^2 = \text{constant} \tag{16}$$

where $\Delta\theta$ is the blade spacing and I is the rothalpy.

Outside of the blade row the angular momentum equation gives:

$$rv_\theta = \text{constant} \tag{17}$$

Equations (16) and (17) can be used with the isentropic relations to show that total conditions are constant outside of the blade row. Evaluating Eq. (15) at some point $()_2$ and using Eq. (17) to eliminate α gives:

$$W_2^2 = \left(\frac{\dot{m}}{\rho_2 r_2 h_2 \Delta\theta}\right) + w_{\theta 2}^2 \qquad (18)$$

Now the isentropic relations and the definition of T_2'' can be used to eliminate ρ_2 giving:

$$\rho_2 = \rho_2'' \left(1 - \frac{W_2^2}{2C_p T_2''}\right)^{\frac{1}{\gamma - 1}} \qquad (19)$$

where

$$\rho_2'' = \rho_1'' \left(\frac{T_2''}{T_1''}\right)^{\frac{1}{\gamma - 1}}$$

Substituting Eq. (19) into Eq. (18) gives:

$$W_2^2 - \varphi_2^2 \left(1 - \frac{W_2^2}{2C_p T_2''}\right)^{\frac{-2}{\gamma - 1}} - w_{\theta 2}^2 = 0 \qquad (20)$$

where

$$\varphi_2 = \frac{\dot{m}}{\rho_2'' r_2 h_2 \Delta\theta}$$

Equation (20) is solved for W_2 at each grid point upstream of the blade using Newton iteration. Other flow quantities are then found using Eq. (17), the known total conditions, and the isentropic relations.

Withing the blade row $rv_\theta \neq$ constant, so Eq. (17) is replaced with an assumption that the flow angle α_2 varies linearly through the blade row. A derivation similar to that above gives:

$$W_2^2 - \varphi_2^2 \left(1 - \frac{W^2}{2C_p T_2''}\right)^{\frac{-2}{\gamma - 1}} = 0 \qquad (21)$$

where

$$\varphi_2 = \frac{\dot{m}}{\rho_2'' r_2 h_2 \cos \alpha_2}$$

which is solved at each grid point within the blade row. Once the flow conditions are known at the trailing edge, Eq. (20) can be used for the downstream region.

Boundary Conditions

At the inlet, total pressure, total temperature, and whirl rv_θ are specified. For subsonic inflow the governing equations have one negative Eigenvalue so that one variable at the inlet must be computed as part of the solution. Here a characteristic relation is used to extrapolate the upstream-running Riemann invariant to the inlet.

The axisymmetric m-momentum equation may be written as:

$$\partial_t R^- + (v_m - a)\partial_m R^- = (v_\theta^2 + a v_m)\, r_m/r + a v_m\, h_m/h \qquad (22)$$

where

$$R^- = v_m - \frac{2a}{\gamma - 1}$$

is the upstream-running Riemann invariant. For steady axisymmetric flow Eq. (22) may be written as:

$$\partial_n R^- = -\left(\frac{\bar{\xi}_\theta}{\bar{h}}\right)\left(\frac{1}{v_m - a}\right)\left[(v_\theta^2 + a v_m)\, r_m/r + a v_m\, h_m/h\right] \qquad (23)$$

Equation (23) is backward-differenced and solved for R^- at the inlet. Then v_m is found from R^- and the specified whirl rv_θ and total temperature T' using:

$$v_m = \frac{(\gamma-1)R^- + \sqrt{(\gamma+1)(4C_p T' - 2v_\theta^2) - 2(\gamma-1)(R^-)^2}}{(\gamma + 1)} \qquad (24)$$

Density and energy are found using isentropic relations.

At the exit the static pressure is specified and the other flow quantities are found using first-order extrapolation. Zeroth-order extrapolation is not usually sufficient in cylindrical coordinate systems because the radius and thus the velocity may change between grid points. For the same reason the inlet and exit boundaries cannot be placed arbitrarily far from the blades. Too small a radius can cause the flow to be supersonic and to large a radius can cause the velocity to approach zero at the boundaries.

Blade surface pressures are found from the normal momentum equation:

$$(\xi_m \eta_m + \bar{\xi}_\theta \bar{\eta}_\theta)\partial_\xi p + (\eta_m^2 + \bar{\eta}_\theta^2)\partial_\eta p = -\rho W^\xi (\eta_m \partial_\xi v_m + \bar{\eta}_\theta \partial_\xi v_\theta) + \rho v_\theta (\eta_m v_\theta - \bar{\eta}_\theta v_m)\, r_m/r \qquad (25)$$

where $W^\xi = 0$ on the surface for viscous flows.

Periodic boundaries are solved like interior points.

Fine-Grid Algorithm

On the fine grid an explicit two-stage finite-difference Runge-Kutta algorithm based on the work of Jameson[15] is used. It is given below as applied to Eq. (7).

Two-stage Runge-Kutta algorithm

$$\hat{q}^{(1)} = \hat{q}^n - \alpha_1 \Delta t R^n$$
$$\hat{q}^{(2)} = \hat{q}^n - \Delta t R^{(1)} \tag{26}$$

where

$$\alpha_1 = 1.2$$

$$R_{i,j} = -\hat{K}_{i,j} + \frac{1}{2}\left[(\hat{F}_{i+1,j} - \hat{F}_{i-1,j}) + (\hat{G}_{i,j+1} - \hat{G}_{i,j-1}) - Re^{-1}(\hat{S}_{i,j+1} - \hat{S}_{i,j-1})\right]$$

Artificial dissipation

$$\hat{q}^{n+1} = \hat{q}^{(2)} + D^{(2)} \tag{27}$$

Collect residuals

$$\Delta\hat{q}^{n+1} = \hat{q}^{n+1} - \hat{q}^n \tag{28}$$

The two-stage scheme given by Eq. (26) has a Courant number limit of one. It is used in preference to a higher-order scheme with a higher Courant number limit because the multigrid scheme used here also has a Courant number limit of one.

Four minor advantages of the Runge-Kutta scheme over the MacCormack scheme are noted:

1. A steady Runge-Kutta solution is independent of the time step while a steady MacCormack solution is not. This is not true when the artificial dissipation is added in a fractional step as in Eq. (27).

2. The centrally-differenced Runge-Kutta scheme produces perfectly symmetric solutions for symmetric problems while the one-sided MacCormack scheme does not.

3. For a two-dimensional problem with centrally-differenced metrics, the Runge-Kutta scheme exactly conserves a free stream while the MacCormack scheme does not. Although the Runge-Kutta scheme is not fully conservative for the quasi-three-dimensional problem because of the source term, it has been found to possess better conservation properties in general.

4. The Runge-Kutta scheme is slightly easier to program than the MacCormack scheme.

Differences in convergence rates between the two schemes are negligible for Courant numbers near one.

Artificial Dissipation

Dissipative terms consisting of second and fourth differences are added to prevent odd-even point decoupling and to allow shock capturing. The dissipative terms are similar to those used by Jameson[15] and others. A one-dimensional version (ξ-direction) is given below. In two dimensions the dissipation is applied as a sequence of one-dimensional operators.

$$D = C(\mu_2 |p_{\xi\xi}| q_{\xi\xi} - \mu_4 q_{\xi\xi\xi\xi}) \tag{29}$$

where

$$C = \frac{\Delta t}{\bar{J}}\sqrt{\bar{n}_m^2 + \bar{n}_\theta^2}$$

$$\mu_2 = O(1)$$

$$\mu_4 = O(1/16)$$

The terms in the coefficient C balance similar terms in Eq. (26). In smooth regions of the flow the dissipative terms are of third order and thus do not detract from the formal second-order accuracy of the fine-grid scheme. In regions of the flow where the second difference of the pressure is large, the second-difference dissipation becomes locally of first order. Note that in other work including Ref. 15 the term $|p_{\xi\xi}|$ is commonly divided by an average pressure. This is not done here because pressures through a centrifugal compressor can increase by factors on the order of five, which would decrease the dissipation correspondingly.

Stability Analysis

A stability analysis of the fine-grid algorithm is performed in two parts. The first part examines the model problem considered by Jameson[15] and is used here to choose the parameters in the two-stage scheme. The model problem is the one-dimensional convection equation with third-order artificial dissipation:

$$q_t + q_x + \mu\Delta x^3 q_{xxxx} = 0 \tag{30}$$

Applying the two stage scheme (Eqs. (26) and (27)) gives:

$$q^{(1)} = q^n - \alpha_1 \frac{\lambda}{2}(q_{j+1} - q_{j-1})^n$$

$$q^{(2)} = q^n - \frac{\lambda}{2}(q_{j+1} - q_{j-1})^{(1)}$$

$$q^{n+1} = q^{(2)} - \mu\lambda(q_{j-2} - 4q_{j-1} + 6q_j - 4q_{j+1} + q_{j+2}) \tag{31}$$

where $\lambda = \Delta t/\Delta x$ is the Courant number.

If we consider a Fourier component of the solution

$$q_j^n = V^n e^{ipx} = V^n e^{ij\xi} \tag{32}$$

where V is the amplitude, p is the wave number, $\xi = p\Delta x$, and $i = \sqrt{-1}$, then the amplification factor is given by:

$$g = \frac{V^{n+1}}{V^n} = [1 - 4\mu\lambda(1 - \cos\xi)^2] \times (1 - \lambda i \sin\xi - \alpha_1\lambda^2 \sin^2\xi) \tag{33}$$

= damping factor x characteristic polynomial for undamped scheme.

The damping coefficient μ is chosen such that $g = 0$ at $\xi = \pi$, giving $\mu = 1/(16\,\lambda)$.

An undamped n-stage scheme can only be stable to $\lambda = n - 1$, so λ is taken to be one while α_1 is chosen. Figure 2 shows a plot of Eq. (33) for several values of α_1, with $\lambda = 1$ and $\mu = 1/(16\,\lambda)$. It can be seen that the two-stage scheme is stable for $0.5 < \alpha_1 \lesssim 1.7$, with $\alpha_1 \approx 1.2$ giving the best damping over the range of frequencies. For $\alpha_1 = 1.2$ and $\mu = 1/(16\,\lambda)$ it can be shown that the two-stage scheme is stable for Courant numbers $\lambda \lesssim 1.1$. In general the two-stage scheme is first-order accurate in time. It is second-order accurate in time only if $\alpha_1 = 0.5$.

The second part of the stability analysis considers the linearized Euler subset of the governing equations (Eqs. (7) and (8)). A Von Neumann analysis shows the stability limit on the time step to be:

$$\Delta t \le \left[W^{\xi} + W^{\eta} + a\sqrt{(\xi_m + \eta_m)^2 + (\bar{\xi}_\theta + \bar{\eta}_\theta)^2} + \frac{v_\theta r_m / r}{2a\sqrt{(\xi_m + \eta_m)^2 + (\bar{\xi}_\theta + \bar{\eta}_\theta)^2}} \right]^{-1}$$

which is implemented as:

$$\Delta t \le \mathrm{CFL} \times \left[|v_m|\,dm + |w_\theta|\,d\bar{\theta} + a\sqrt{dm^2 + d\bar{\theta}^2} + \frac{v_\theta r_m / r}{2a\sqrt{dm^2 + d\bar{\theta}^2}} \right]^{-1} \qquad (34)$$

where

$$dm = |\xi_m| + |\eta_m|$$

$$d\bar{\theta} = |\bar{\xi}_\theta| + |\bar{\eta}_\theta|$$

A spatially-variable time-step $\Delta t_{i,j}$ is used in the two-stage scheme (Eqs. (26) and (27)) to accelerate convergence to steady state. Equation (34) is used to choose the time step at each grid point such that the Courant number is constant, typically CFL = 0.95. Time steps are calculated based on the initial conditions. They are stored and not updated during the calculations.

Multigrid Algorithm

The multigrid algorithm originated by Ni[16] and modified by Johnson and Chima[17-19] is used to accelerate convergence of the fine-grid algorithm. Ni's scheme is basically a one-step Lax-Wendroff scheme applied on a coarse grid. Ni used it to accelerate his own fine-grid Euler scheme.[16] Johnson adapted Ni's method to other fine-grid schemes including MacCormack's scheme.[17] He also used it for viscous flows by demonstrating that dissipative terms need not be included on the coarse grids. Thus the multigrid scheme used here is based solely on the Euler equations. It is entirely independent of the viscous terms, the turbulence model, and the artificial dissipation used on the fine grid.

One-step Lax-Wendroff schemes including Ni's scheme require temporal derivatives of the flux vectors. These terms are computed as the Jacobian matrix of the flux vector times the temporal difference of the solution vector. Johnson replaced these lengthy computations with a direct temporal difference of the flux vector using the old and new solutions on the fine grid.[18] This "flux based" scheme is considerably simpler than Ni's original scheme.

The flux-based multigrid scheme is derived by expanding the fine-grid change Δq^{n+1}, (Eq. (28)), in a Taylor series.

$$\Delta\hat{q}^{n+2} = \Delta\hat{q}^{n+1} + \Delta t(\Delta\hat{q}^{n+1})_t + O(\Delta t^2)$$

The Euler equations are used to replace the third term.

$$(\Delta\hat{q}^{n+1})_t = [\Delta t(\hat{K} - \hat{F}_\xi - \hat{G}_\eta)]_t \qquad (35)$$

Interchanging the space and time derivatives and using backward differencing in time gives:

$$(\Delta\hat{q}^{n+1})_t = \Delta t(\hat{K}_t - \hat{F}_{t\xi} - \hat{G}_{t\eta})$$

$$= (\hat{K}^{n+1} - \hat{K}^n) - (\hat{F}^{n+1} - \hat{F}^n)_\xi - (\hat{G}^{n+1} - \hat{G}^n)_\eta$$

and finally

$$\Delta\hat{q}^{n+2} = \Delta\hat{q}^{n+1} + \Delta t\left[\Delta\hat{K} - (\Delta\hat{F})_\xi - (\Delta\hat{G})_\eta\right]^{n+1} \qquad (36)$$

where

$$\Delta\hat{K}^{n+1} = \hat{K}(q^{n+1}) - \hat{K}(q^n), \text{ etc.}$$

Equation (36) is implemented on a coarse grid with spacing $\ell\Delta\xi$, and $\ell\Delta\eta$, and time step $\ell\Delta t_{i,j}$, $\ell = 1, 2, 4, 8, \ldots$, using:

$$\Delta\hat{q}^{n+2} = \frac{1}{4}\left\{ \left[\Delta\hat{q} + \Delta t_{i,j}(\ell\Delta\hat{K} - \Delta\hat{F} - \Delta\hat{G})\right]_{i+\ell,j+\ell} + \left[\Delta\hat{q} + \Delta t_{i,j}(\ell\Delta\hat{K} - \Delta\hat{F} + \Delta\hat{G})\right]_{i+\ell,j-\ell} + \left[\Delta\hat{q} + \Delta t_{i,j}(\ell\Delta\hat{K} + \Delta\hat{F} - \Delta\hat{G})\right]_{i-\ell,j+\ell} + \left[\Delta\hat{q} + \Delta t_{i,j}(\ell\Delta\hat{K} + \Delta\hat{F} + \Delta\hat{G})\right]_{i-\ell,j-\ell} \right\}^{n+1} \qquad (37)$$

Fine-grid changes $\Delta\hat{q}^{n+1}$ are restricted to the coarse grid by injection. The multigrid algorithm (Eq. (37)) computes coarse-grid corrections $\Delta\hat{q}^{n+2}$ based on changes in the fine-grid solution. Thus the coarse-grid corrections must vanish if the fine-grid solution converges, thereby retaining fine-grid accuracy.

The coarse-grid corrections are prolonged back to the fine grid using bilinear interpolation and the fine-grid solution is updated. The process may then be repeated on a coarser grid.

Vectorization

The explicit Runge-Kutta and multigrid algorithms used here have been highly vectorized for the Cray I-S at NASA Lewis Research Center. Indeed the Runge-Kutta computations were clocked at about 40 million floating point operations/sec (40 mflops) for an Euler solution on a 113 by 25 grid. The efficiency of the multigrid computations decreases as the grid gets coarser and the vectors get shorter.

The code was redimensioned for each grid size run and required 260 K words of memory for the largest grid (161 by 33). The quasi-three-dimensional code requires about 20 percent more storage than the two-dimensional code.[6]

Results

Results are presented for the following problems: a cascade of thin flat plates with round leading edges, a centrifugal impeller, and a vaned-radial diffuser. Both Euler and Navier-Stokes results are presented.

To aid in developing the quasi-three-dimensional code and to illustrate the capabilities of the analysis, a model problem was developed representing a cascade of thin flat plates with round leading edges. The plate has unit chord, four percent thickness, and a pitch of 0.7. Figure 3 shows the computational grid around the plate. The inviscid flow grid had 113 by 25 points with 5° spacing around the leading edge circle and a normal spacing of 1.8×10^{-4}. The viscous flow grid had 113 by 33 points with a normal spacing of 5×10^{-5}. The grid shown in Fig. 3, and most of the subsequent grid and contour plots in this paper, are drawn in a transformed plane in which the abscissa is $\int dm/r$ and the ordinate is θ. This transformation preserves angles and is discussed in Ref. 10.

Grids are generated in an $(m, \bar{r}\theta)$ coordinate system where $\bar{r}$ is some mean radius, and are independent of the local radius r and stream-surface thickness h. Values of r and h are supplied to the quasi-three-dimensional code later and can be varied to simulate different geometries.

A flat cascade was simulated by setting r = constant and h = constant. Figure 4 shows static pressure contours for an Euler solution with an inlet Mach number of 0.33. (Titles on the figures give nominal values of Mach number, Reynolds number, and flow angle based on the leading-edge velocity triangles given as input. Actual inlet conditions may change as the solution develops.) The contours show the stagnation region and a mild acceleration due to blockage. Identical results were obtained using the two-dimensional code.[6] The solution was run 5000 cycles with two multigrid levels and took 165 sec on the Cray. The residuals were reduced eight decades so the solution could have been stopped at about 2000 cycles with a three-decade reduction in the residuals.

A radial duct with constant cross-sectional area was simulated by setting $r = m$ and $r \times h$ = constant. The solution is identical to the flat cascade results shown in Fig. 4.

A radial diffuser with 36 blades was simulated by setting $r = m$ and h = constant. Figure 5 shows static pressure contours for an Euler solution with an inlet Mach number of 0.38 and an exit Mach number of 0.27. The plot is shown in polar coordinates. The contours show the diffusion of the flow due to the area change. The solution was run 2500 cycles with two multigrid levels and took 92 sec on the Cray. The residuals were reduced 6 decades so the solution could have been stopped at about 1250 cycles with a three-decade reduction in the residuals.

A centrifugal impeller with 36 blades was simulated by setting $r = m$, h = constant, and a rotation rate of 1000 rad/sec (9550 rpm). Figure 6 shows Mach number contours for a turbulent solution with an inlet Mach number of 0.5 and an exit Mach number of 0.41. The impeller produces a total pressure ratio of 1.05. The plot is shown in polar coordinates with rotation upwards. The inlet whirl is zero but because of the rotation the inlet relative flow angle is 10.6°. This incidence desymmetrizes the flow and produces a pressure loading on the blade. At the exit this loading conflicts with the specified exit pressure and is responsible for the kinks in the contours there.

Figure 7 shows convergence histories for the previous example with various levels of multigrid. Convergence is taken to be a three decade drop in the maximum residual to 2×10^{-5}. For this example two grids are 1.64 times faster than the fine grid and three grids are 3.12 times faster than the fine grid. CPU times are included on the figure.

The remaining results are for a nominally 6:1 total-pressure ratio centrifugal impeller and a matching vaned-radial diffuser. These components were designed by the Air Force for use in an auxilliary power unit and were modified and tested at NASA Lewis Research Center. The compressor has a diameter of 16.1 cm. It has 19 blades and was designed for a total pressure ratio of 5.9:1 with a mass flow of 1.033 kg/sec at 68 384 rpm. The diffuser has 27 blades and a diameter of 25.1 cm. Further details concerning the components can be be found in Ref. 25.

Figure 8 shows the computational grid used for the impeller. The grid has 161 by 33 points (161 by 17 shown) with a normal spacing of 3×10^{-4} cm for inviscid flows and 5×10^{-5} cm for viscous flows. The leading edge is round with a radius of 0.045 cm and the grid points are 7° apart.

Figure 9 shows normalized radius (RMSP = r), stream-surface thickness (BESP = h), and their product (R*B = rh) versus fraction of impeller chord. These values were taken from a meridional analysis.[8]

Euler and Navier-Stokes solutions were each run 2000 cycles with two multigrid levels, reducing the maximum residual three decades. The Euler solution took 117 sec and the Navier-Stokes solution took 185 sec on the Cray.

Surface static pressure distributions for the impeller are compared in Fig. 10. Three solutions with identical mass flows are shown: an Euler solution (dashed), a Navier-Stokes solution (solid), and a panel solution (circles,[10]). The Euler and Navier-Stokes solutions were run with various exit pressures until the desired mass flow was obtained. The shapes of the three pressure distributions are similar but the panel solution has higher pressure levels since it is loss-free. The Euler solution has strong shock losses which lower the pressure levels. The Navier-Stokes solution has weaker shocks due to viscous smoothing of the leading edge, but blockage effects decrease the pressure levels overall.

Figure 11 shows relative Mach number contours for the Euler solution. The dashed line is the sonic line. At the inlet the relative Mach number is 0.91. At the leading edge the flow has 10° of incidence. This produces a large supersonic bubble with a peak Mach number of 1.92 on the suction (upper) surface. The bubble terminates with a normal shock that is smeared due to grid shearing in this region. There is also a tiny supersonic bubble on the pressure (lower) surface which is not visible at this scale.

Some interesting flow phenomena evident in Fig. 11 can be explained by the concept of a relative eddy. The flow through an impeller is predominantly inviscid and tends to remain irrotational. The blade row in Fig. 11 is rotating downward and so adds clockwise vorticity to the flow. To remain irrotational the flow develops a counterclockwise circulation within the passage. Thus the flow can be modelled as a superposition of a through-flow component and a component rotating counter to the blade row called a relative eddy. The effect of the relative eddy is to accelerate the flow on the suction surface and decelerate the flow on the pressure surface as can be seen in Fig. 11.

A more dramatic effect of the relative eddy is to sweep the unconfined flow beyond the trailing edge up and away from the blade in a spiral, with a slip line leaving the trailing edge. As a common example of slip from rotating machinery, consider the flow of water from a lawn sprinkler as viewed rotating with the sprinkler. The flow spirals up and opposite to the rotation of the sprinkler. It is emphasized that this is strictly an inviscid phenomena.

Figure 12 shows relative Mach number contours for a Navier-Stokes solution for the impeller. Here viscous effects reduce the peak suction-surface Mach number to 1.72 and the peak pressure-surface Mach number to just over 1.0. Both surfaces have small leading-edge separation bubbles that are barely resolved on this grid. The pressure surface quickly develops a thick boundary layer and the suction-surface boundary layer thickens after the shock. This blockage causes the viscous pressure levels to be lower than the inviscid levels in Fig. 10. The rotation energizes and diminishes the boundary layers on the radial portions of the blade.

Here again the relative eddy sweeps the flow off the trailing edge in a spiral. Since the flow does not follow the grid lines the thin-layer assumption may be invalid and diffusion across the wake may not be properly accounted for. This is one shortcoming of the present analysis. However, since the trailing-edge slip is an inviscid phenomena it is felt that the character of the solution is correct.

Figure 13 shows the computational grid for the radial diffuser vane. The grid has 145 by 33 points (145 by 17 shown) with a normal spacing of 2.5×10^{-4} cm for inviscid flows and 6×10^{-5} cm for viscous flows. The round leading edge has a radius of 0.025 cm and the grid points are 7° apart. At the trailing edge the actual vane is cut off at constant radius and the duct turns axially. For this analysis the trailing edge was sharpened and the duct was extended radially.

Figure 14 shows the normalized radius and stream-surface thickness versus fraction of vane chord. These values were taken from a combined meridional/boundary-layer analysis.[8,9] Although the vanes have constant height, boundary layer blockage decreases the flow area by nearly 50 percent.

An Euler solution was run 4000 cycles with two multigrid levels, taking 214 sec on the Cray. A Navier-Stokes solution was run 2000 cycles with three multigrid levels, taking 179 sec. In each case the maximum residual was reduced three decades.

Surface static pressure distributions for the diffuser vane are compared in Fig. 15. Again, panel, Euler, and Navier-Stokes solutions are compared. The shapes of the pressure distributions are similar but the panel solution has higher pressure levels since it is loss-free. The Euler and Navier-Stokes solutions each have small supersonic bubbles terminated by normal shocks near the leading edge, and the losses lower the pressure levels. Additional blockage effects cause the viscous pressure levels to be even lower than the inviscid levels.

Figure 16 shows Mach number contours for the Euler solution. The inlet Mach number is exactly 1.0 but the radial component is only 0.29 so the flow is subsonic in character. Because of the increasing radius the total Mach number drops to about 0.83 near the leading edge. The flow has a slight positive incidence at the leading edge and the flow accelerates to a peak Mach number of about 1.5 on the suction surface. The tiny supersonic bubble (visible only as a black dot at this scale) terminates with a shock at about 0.26 percent chord. The pressure surface develops an even smaller supersonic bubble. The diffusion through the passage is evident in Fig. 16.

Figure 17 shows Mach number contours for the Navier-Stokes solution. Here viscous effects at the leading edge entirely suppress the formation of supersonic bubbles. The thick boundary layers that develop in the diffuser are obvious, but the flow remains attached on both surfaces.

Concluding Remarks

A quasi-three-dimensional Euler and Navier-Stokes analysis technique has been developed for blade-to-blade flows in turbomachinery. The analysis solves the thin-layer Navier-Stokes

equations written in general coordinates for an axisymmetric stream surface, and accounts for the effects of blade-row rotation, radius change, and stream-surface thickness. It is believed that this is the first Navier-Stokes analysis to include these effects.

The solution technique is a two-stage Runge-Kutta scheme based on the work of Jameson. Efficiency is achieved through use of vectorization, a spatially-variable time-step, and a multigrid scheme based on Johnson's revisions of Ni's scheme. The multigrid scheme typically reduces the CPU time required by the fine grid scheme alone by a factor of about three, for both inviscid and viscous flows.

Results for a model problem show the analysis to be viable for a variety of axial, radial, and rotating geometries. Results for a centrifugal impeller and a radial diffuser vane show that the analysis can predict a number of phenomena that are not accounted for in previous analyses. These phenomena include: leading-edge stagnation points, leading-edge separation, supersonic regions and shocks, blade-surface boundary layer growth, and trailing-edge slip lines.

It is thought that the ability to predict these phenomena rapidly for general geometries could make the quasi-three-dimensional analysis a useful tool for turbomachinery design. Furthermore the quasi-three-dimensional analysis can provide insight into both physical and numerical problems that can be expected with fully three-dimensional problems in the future.

References

1. McFarland, E.R., "Solution of Plane Cascade Flow Using Improved Surface Singularity Methods," Journal of Engineering for Power, Vol. 104, No. 3, July 1982, pp. 668-674.

2. Ives, D.C., and Liutermoza, J.F., "Second-Order-Accurate Calculation of Transonic Flow over Turbomachinery Cascades," AIAA Journal, Vol. 17, No. 8, Aug. 1979, pp. 870-876.

3. Denton, J.D., "An Improved Time Marching Method for Turbomachinery Flow Calculation," Journal of Engineering for Power, Vol. 105, No. 3, July 1983, pp. 514-524.

4. Subramanian, S.V., and Bozzola, R., "Applica- tion of Runge Kutta Time Marching Scheme for the Computation of Transonic Flows in Turbo- machines," AIAA Paper 85-1332, July 1985.

5. Steger, J.L., Pulliam, T.H., and Chima, R.V., "An Implicit Finite-Difference Code for Inviscid and Viscous Cascade Flow," AIAA Paper 80-1427, July 1980.

6. Chima, R.V., "Analysis of Inviscid and Viscous Flows in Cascades with an Explicit Multiple-Grid Algorithm," AIAA Paper 84-1663, June 1984.

7. Wu, C.-H., "A General Theory of Three-Dimensional Flow in Subsonic and Supersonic Turbomachines of Axial-, Radial-, and Mixed-Flow Types," NACA TN-2604, 1952.

8. Katsanis, T., and McNally, W.D., "Revised FORTRAN Program for Calculating Velocities and Streamlines on the Hub-Shroud Midchannel Stream Surface of an Axial-, Radial-, or Mixed-Flow Turbomachine or Annular Duct, I - User's Manual," NASA TN-D-8430, 1977.

9. McNally, W.D., "FORTRAN Program for Calculating Compressible Laminar and Turbulent Boundary Layers in Arbitrary Pressure Gradients," NASA TN-D-5681, 1970.

10. McFarland, E.R., "A Rapid Blade-to-Blade Solution for Use in Turbomachinery Design," Journal of Engineering for Gas Turbines and Power, Vol. 106, No. 2, Apr. 1984, pp. 376-382.

11. Katsanis, T., "FORTRAN Program for Calculating Transonic Velocities on a Blade-to-Blade Stream Surface of a Turbomachine," NASA TN-D-5427, 1969.

12. Farrell, C., and Adamczyk, J., "Full Potential Solution of Transonic Quasi-3-D Flow Through a Cascade Using Artificial Compressibility," Journal of Engineering for Power, Vol. 104, No. 1, Jan. 1982, pp. 143-153.

13. Bertheau, F., Ribaud, Y., and Millour, V., "Transonic Blade-to-Blade Calculations in an Axial, Radial, or Mixed Flow Cascade Equipped with Splitter Blades," ASME Paper 85-GT-86, Mar. 1985.

14. MacCormack, R.W., "The Effect of Viscosity in Hypervelocity Impact Cratering," AIAA Paper 69-354, Apr. 1969.

15. Jameson, A., and Baker, T.J., "Multigrid Solution of the Euler Equations for Aircraft Configurations," AIAA Paper 84-0093, Jan. 1984.

16. Ni, R.H., "A Multiple Grid Scheme for Solving the Euler Equations," AIAA Paper 81-1025, AIAA 5th Computational Fluid Dynamics Conference, June 1981, pp. 257-264.

17. Johnson, G.M., "Convergence Acceleration of Viscous Flow Computations," NASA TM-83039, 1982.

18. Johnson, G.M., "Flux-Based Acceleration of the Euler Equations," NASA TM-83453, 1983.

19. Chima, R.V., and Johnson, G.M., "Efficient Solution of the Euler and Navier-Stokes Equations with a Vectorized Multiple-Grid Algorithm," AIAA Journal, Vol. 23, No. 1, Jan. 1985, pp. 23-32.

20. Katsanis, T., "Applications of the Contravariant Form of the Navier-Stokes Equations," NASA TM-83448, 1983.

21. Baldwin, B.S., and Lomax, H., "Thin-Layer Approximation and Algebraic Model for Separated Turbulent Flows," AIAA Paper 78-257, Jan. 1978.

22. Sorenson, R.L., "A Computer Program to Generate Two-Dimensional Grids About Airfoils and Other Shapes by the Use of Poisson's Equation," NASA TM-81198, 1980.

23. Steger, J.L., and Sorenson, R.L., "Automatic Mesh-Point Clustering Near a Boundary in Grid Generation with Elliptic Partial Differential Equations," Journal of Computational Physics, Vol. 33, No. 3, Dec. 1979, pp. 405-410.

24. Barton, J.T., and Pulliam, T.H., "Airfoil Computation at High Angles of Attack, Inviscid and Viscous Phenomena," AIAA Paper 84-0524, Jan. 1984.

25. Klassen, H.A., Wood, J.R., and Schumann, L.F., "Experimental Performance of a 16.10-Centimeter-Tip-Diameter Sweptback Centrifugal Compressor Designed for a 6:1 Pressure Ratio," NASA TM X-3552, 1977.

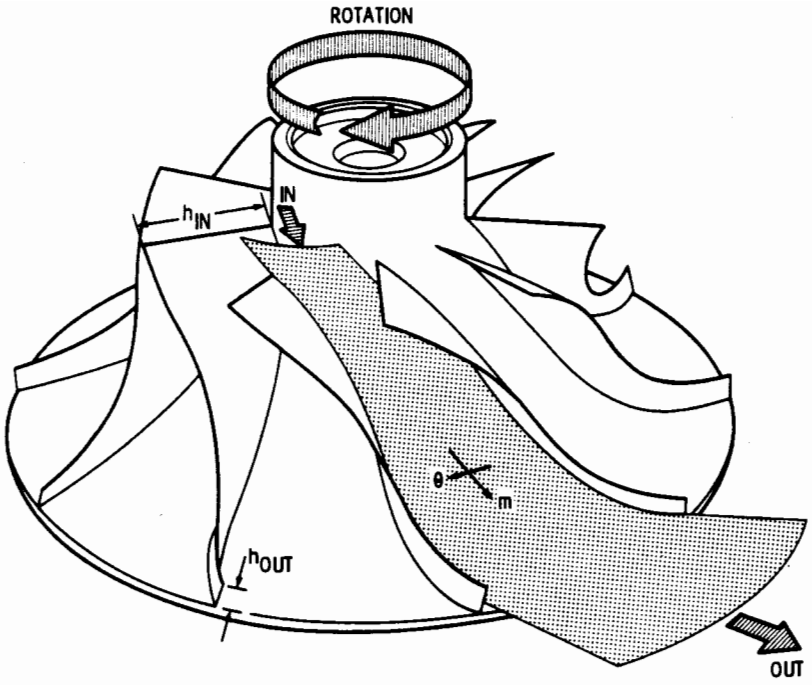

Figure 1. - Quasi-three-dimensional stream surface and coordinate system for a centrifugal compressor.

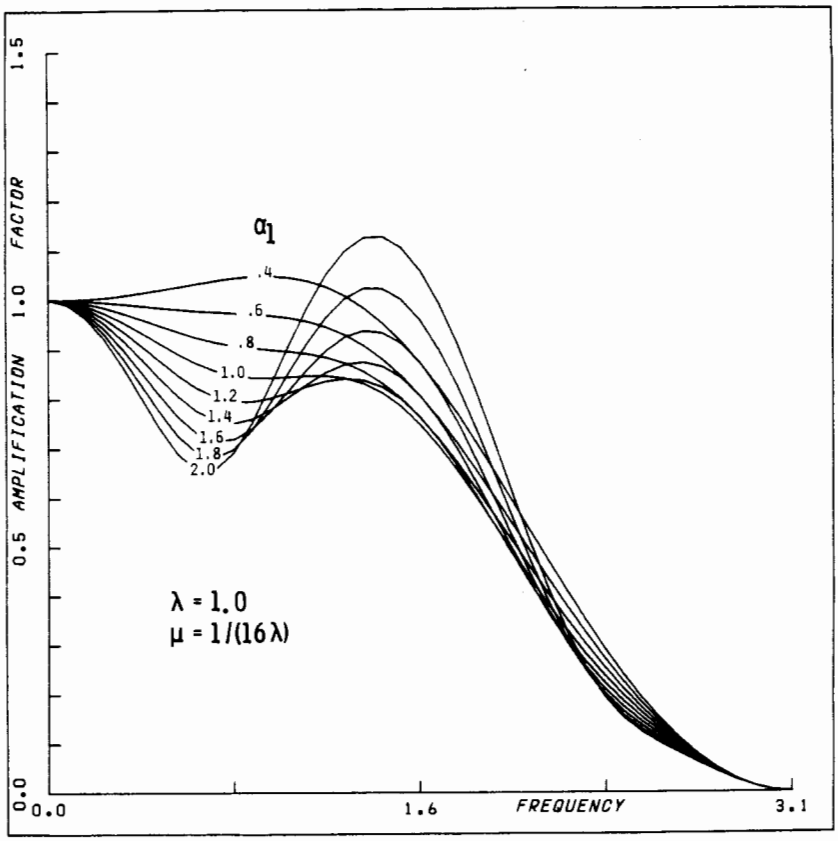

Figure 2. - Amplification factor for two-stage Runge-Kutta scheme.

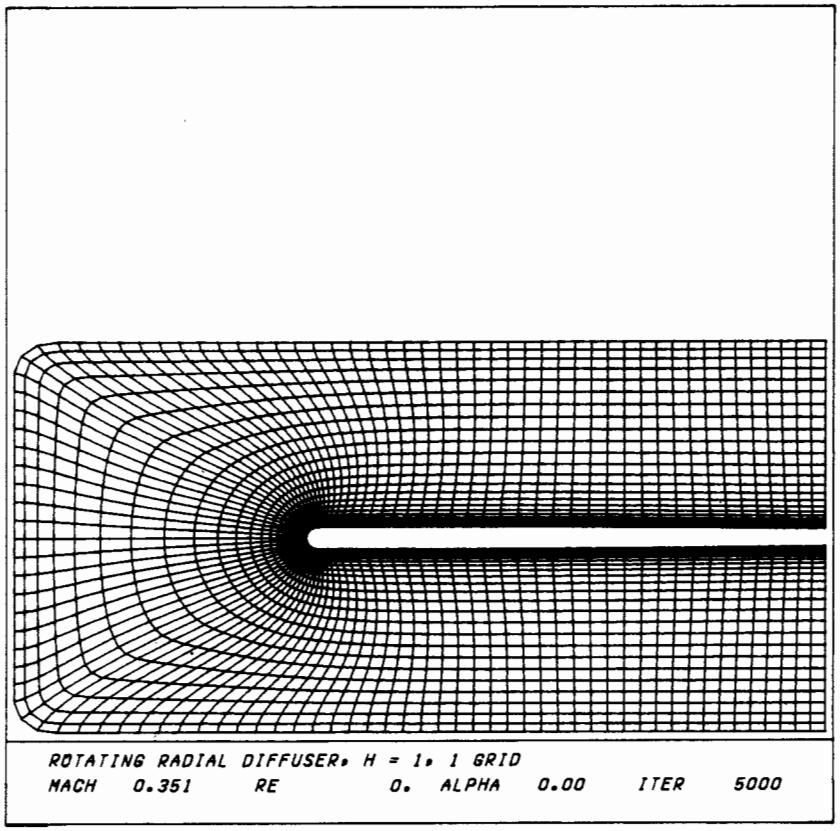

Figure 3. - Computational grid for flat plate model problem.

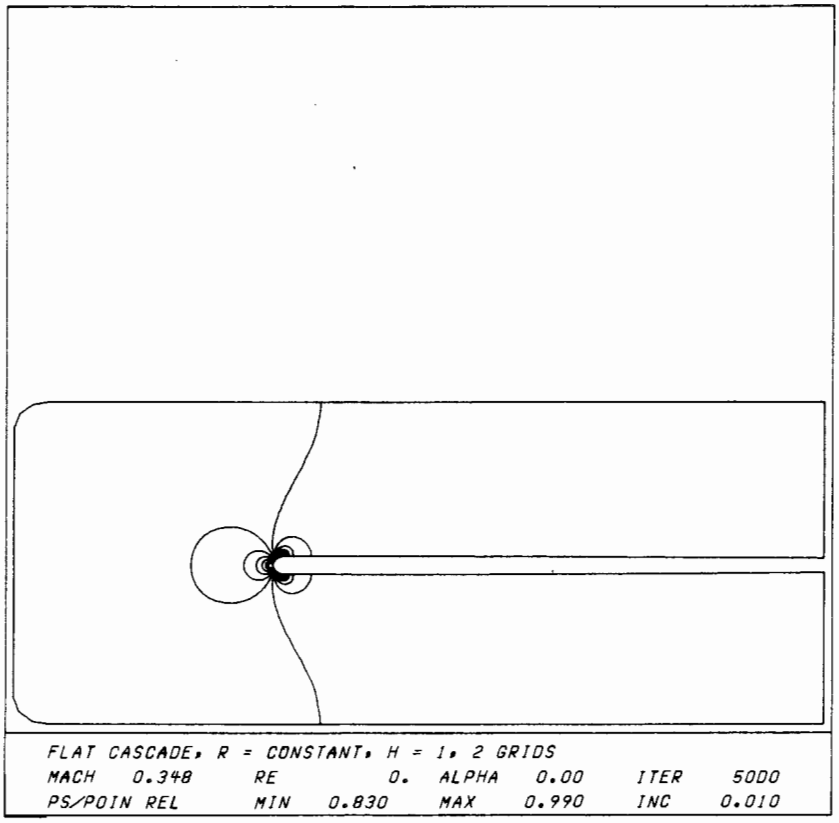

Figure 4. - Static pressure contours for inviscid flat plate cascade model.

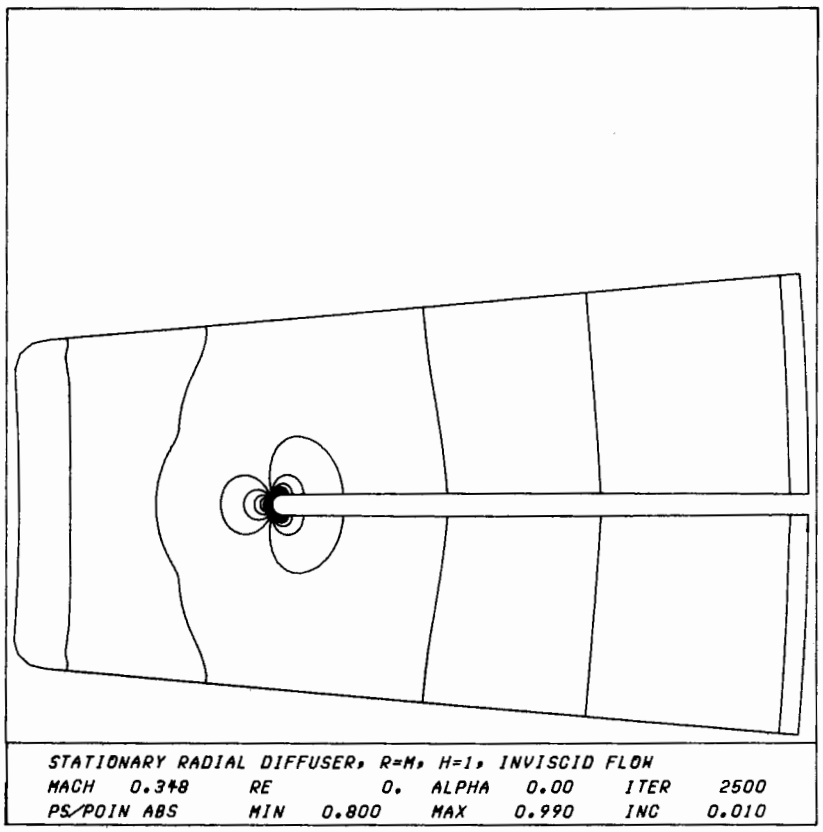

Figure 5. - Static pressure contours for inviscid radial diffuser model.

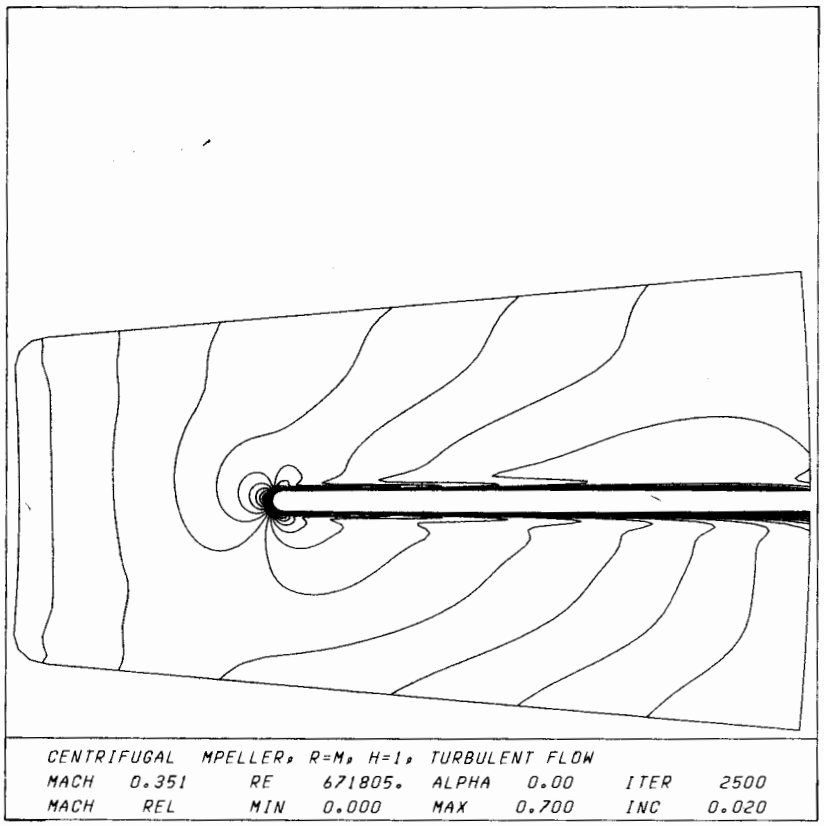

Figure 6. - Mach number contours for turbulent centrifugal impeller model.

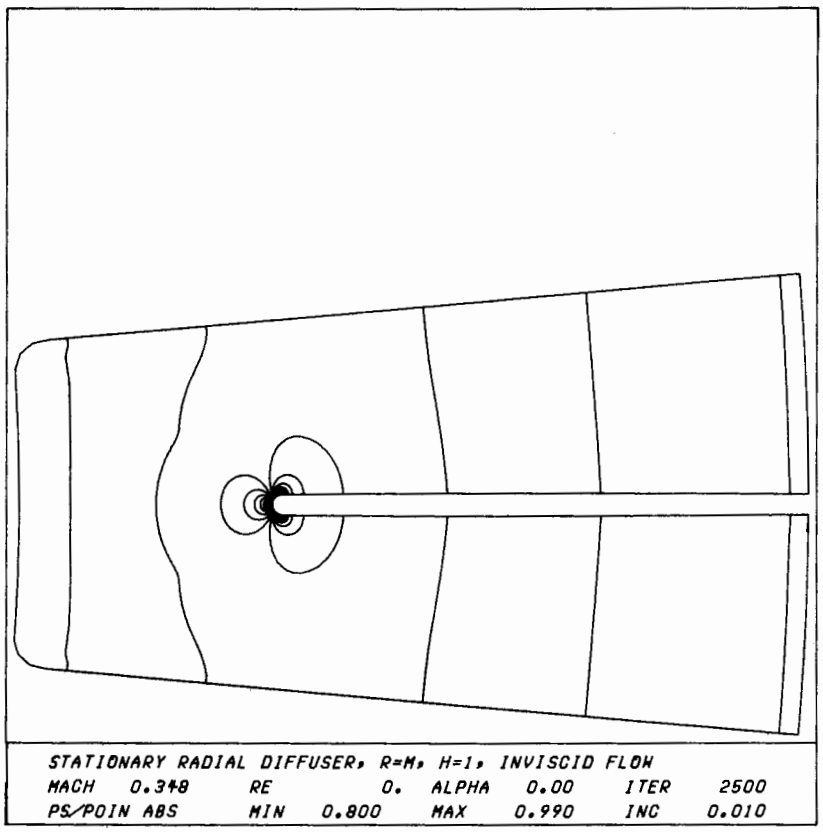

Figure 5. - Static pressure contours for inviscid radial diffuser model.

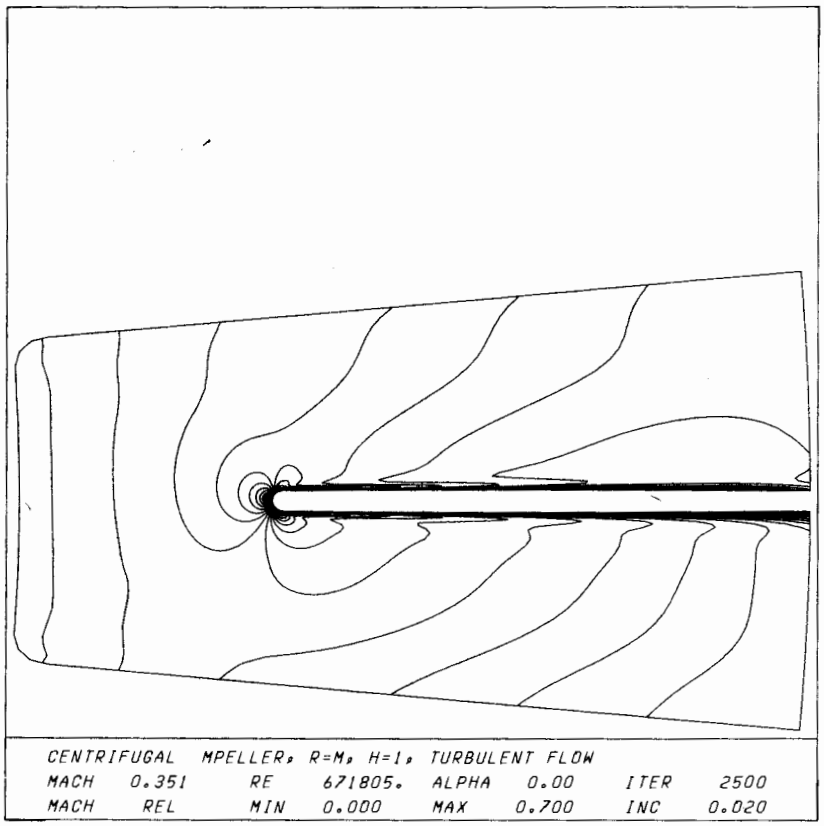

Figure 6. - Mach number contours for turbulent centrifugal impeller model.

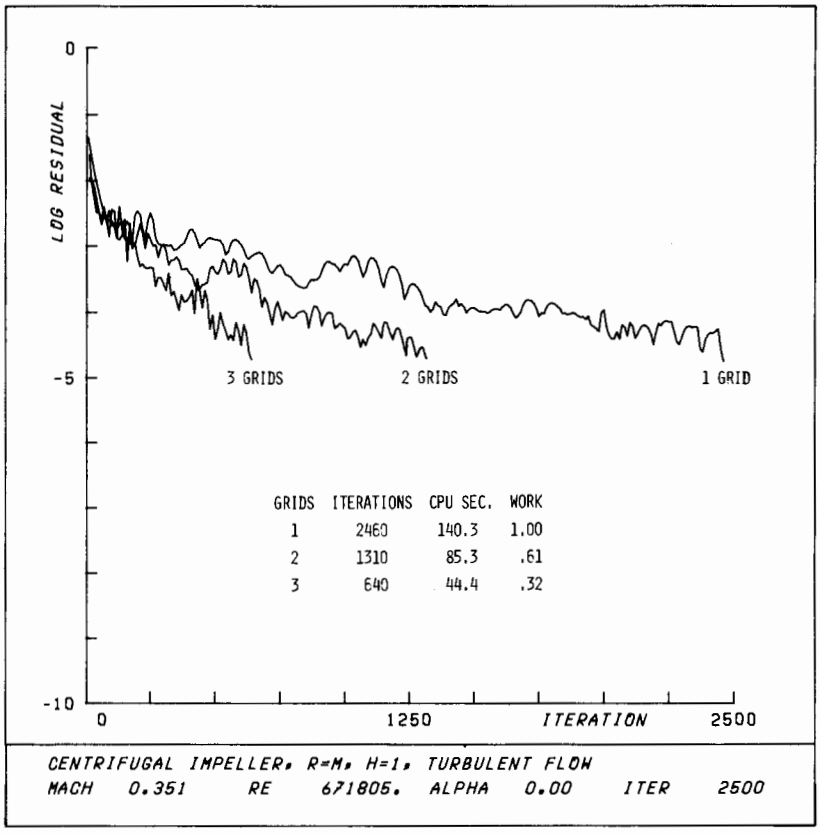

Figure 7. - Multigrid convergence histories for turbulent centrifugal impeller model.

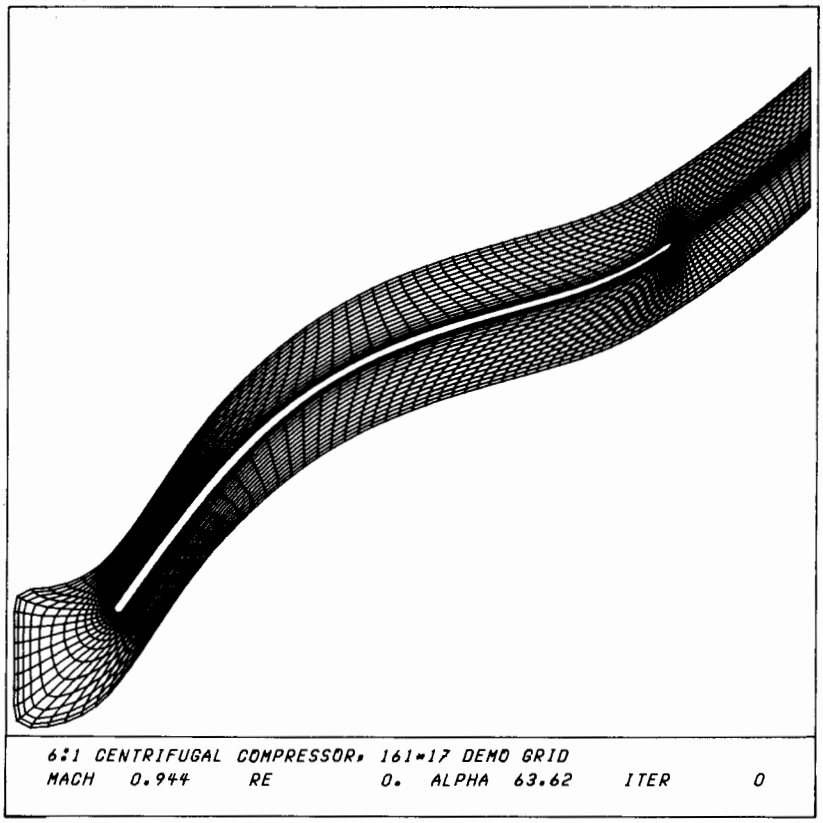

Figure 8. - Computational grid for 6:1 pressure ratio centrifugal impeller.

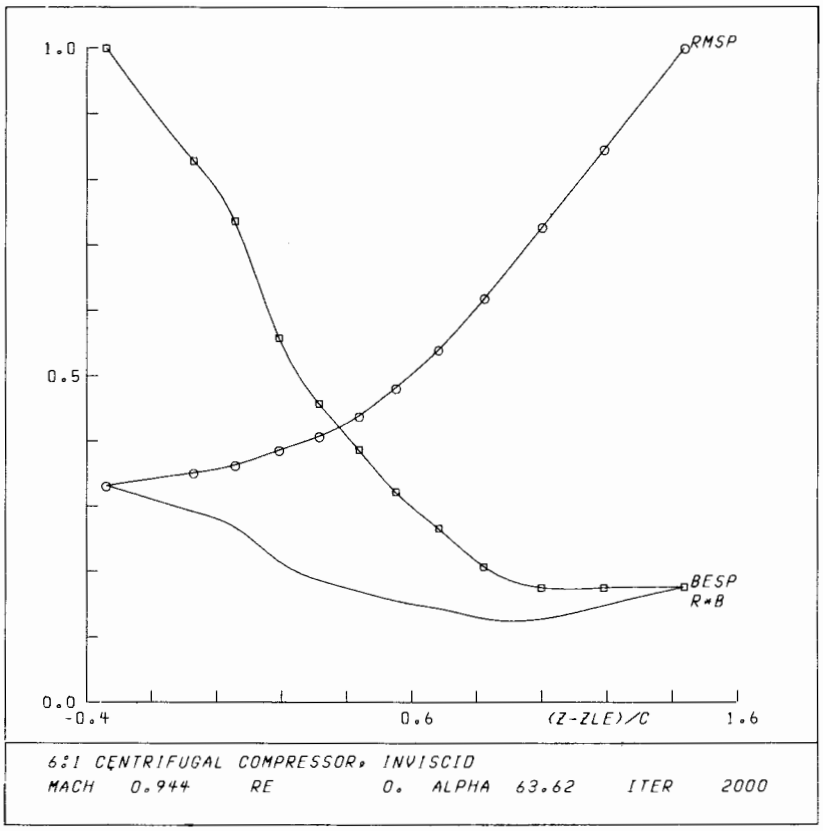

Figure 9. - Radius (RMSP) and stream surface thickness (BESP) for 6:1 centrifugal impeller.

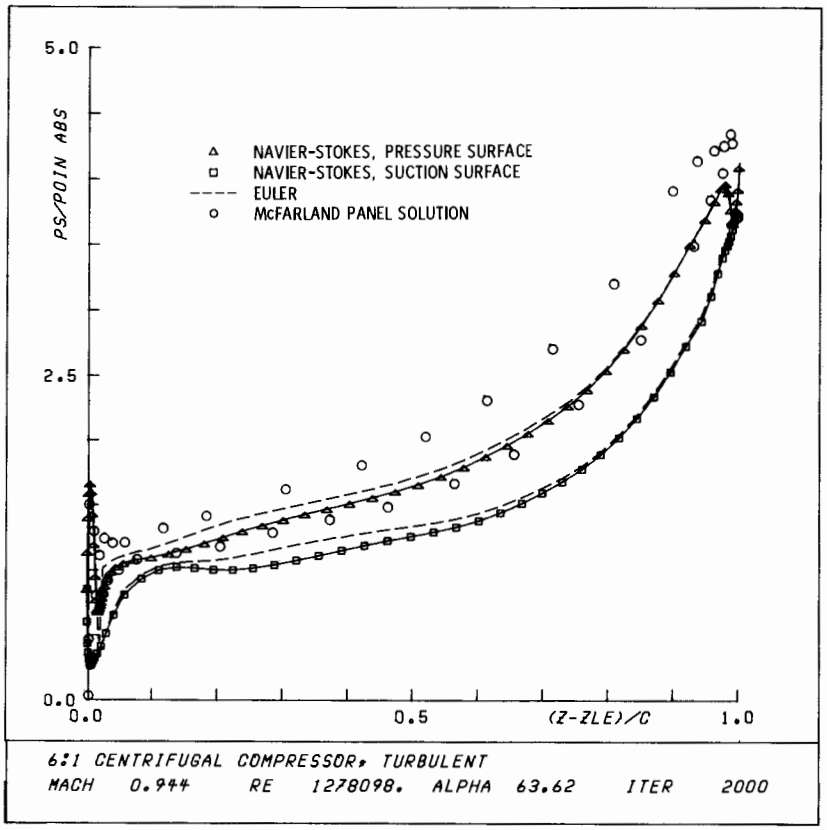

Figure 10. - Static pressure distribution for 6:1 centrifugal impeller.

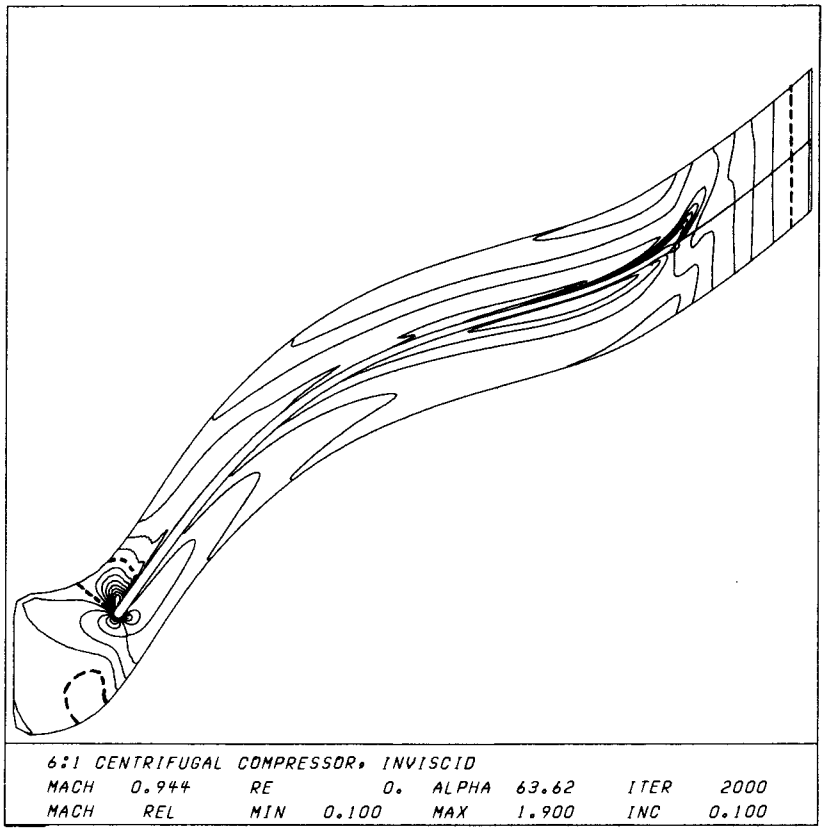

Figure 11. - Mach number contours for inviscid flow in 6:1 centrifugal impeller.

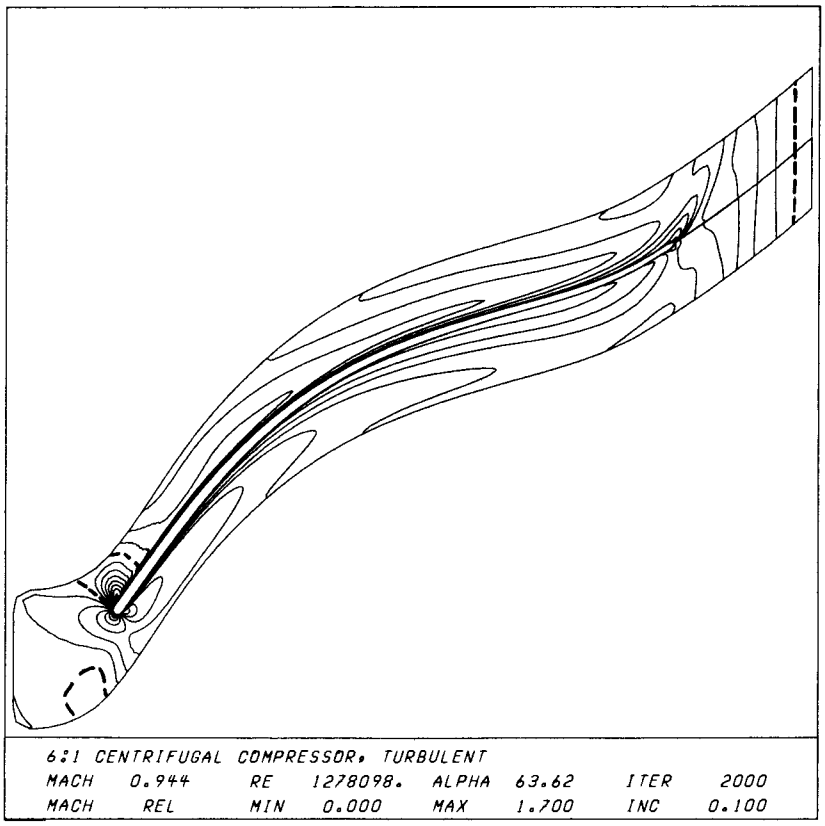

Figure 12. - Mach number contours for turbulent flow in 6:1 centrifugal impeller.

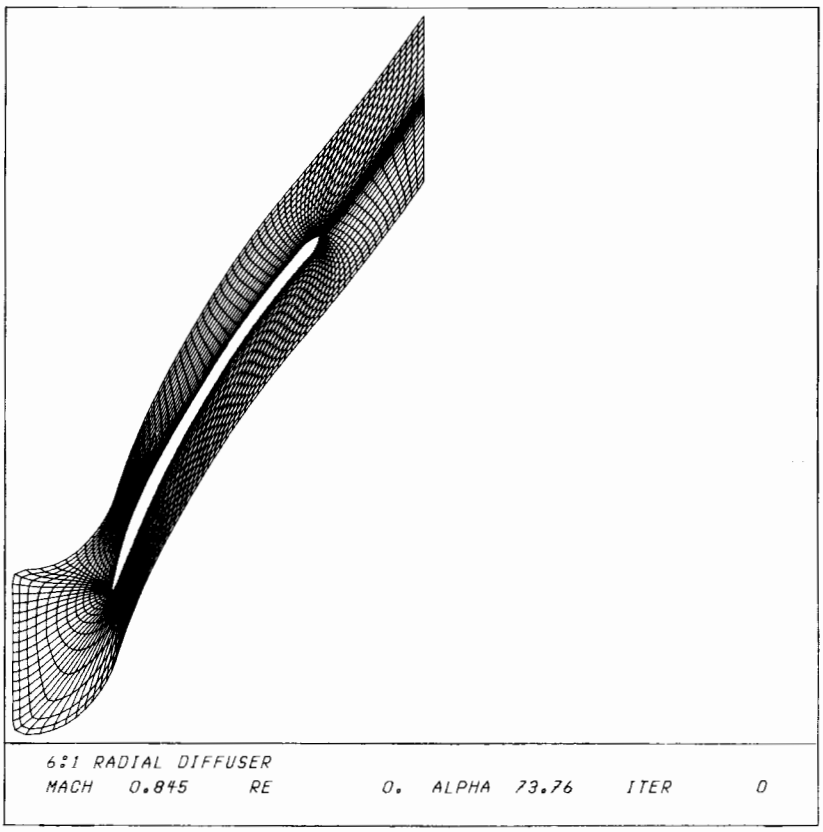

Figure 13. - Computational grid for 6:1 pressure ratio radial diffuser.

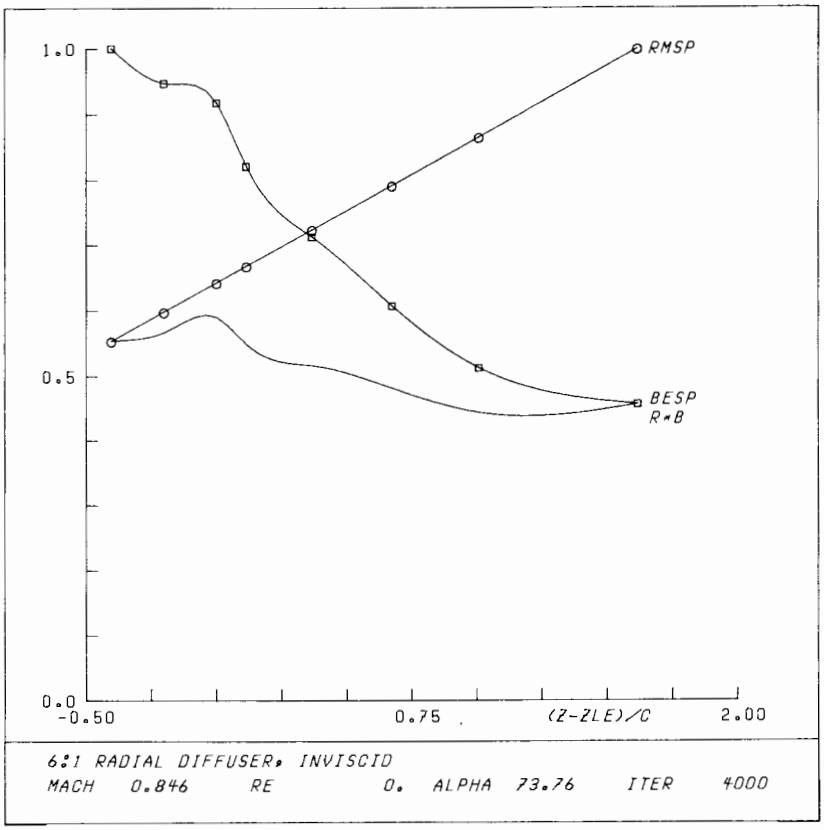

Figure 14. - Radius (RMSP) and stream surface thickness (BESP) for 6:1 radial diffuser.

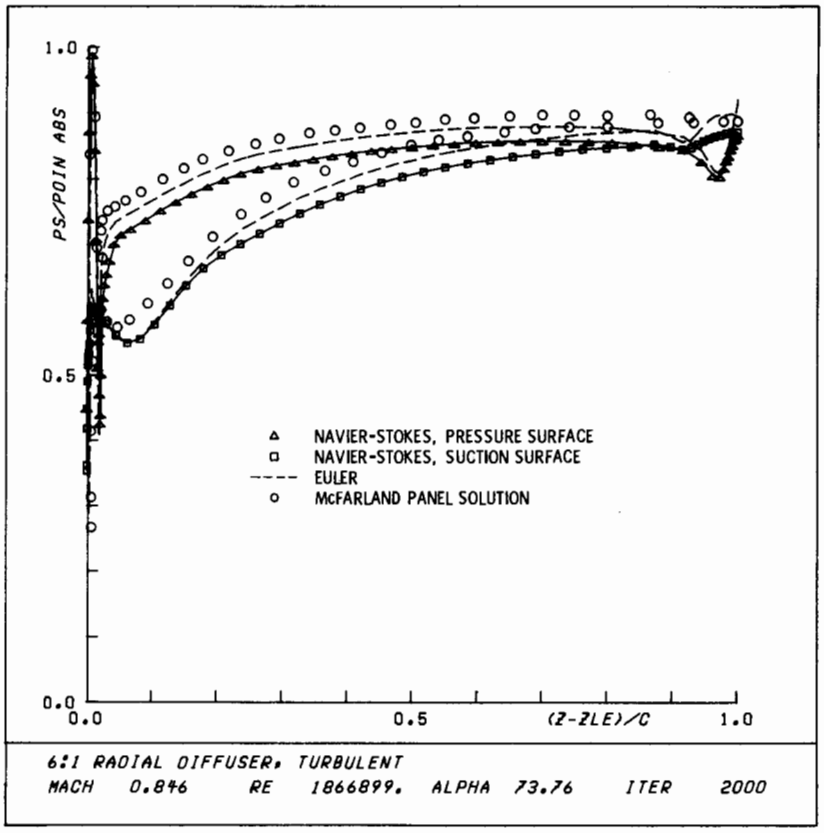

Figure 15. - Static pressure distribution for 6:1 radial diffuser.

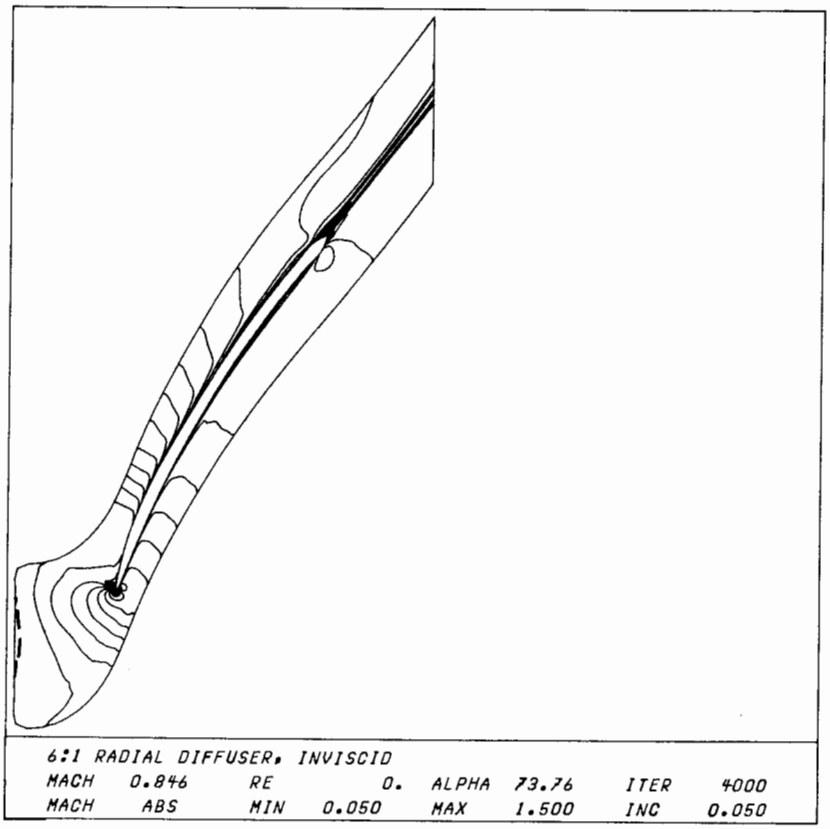

Figure 16. - Mach number contours for inviscid flow in 6:1 radial diffuser.

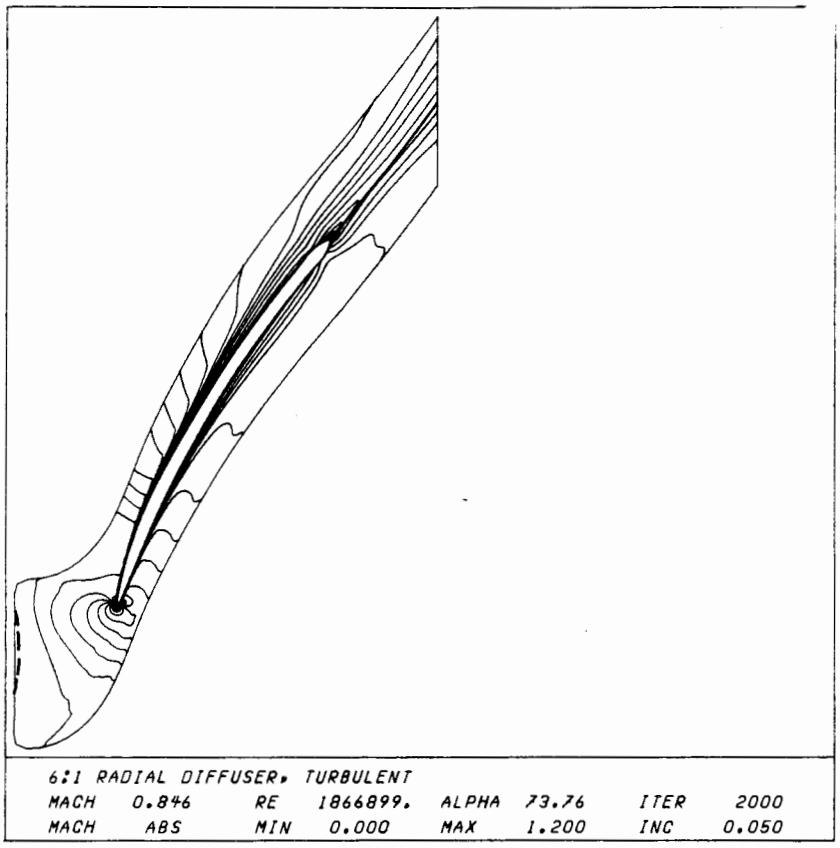

Figure 17. - Mach number contours for turbulent flow in 6:1 radial diffuser.

1. Report No.	2. Government Accession No.	3. Recipient's Catalog No.
NASA TM-87128		

4. Title and Subtitle	5. Report Date
Development of An Explicit Multigrid Algorithm for Quasi-Three-Dimensional Viscous Flows in Turbomachinery	6. Performing Organization Code: 505-31-04

7. Author(s)	8. Performing Organization Report No.
Rodrick V. Chima	E-2681
	10. Work Unit No.

9. Performing Organization Name and Address	11. Contract or Grant No.
National Aeronautics and Space Administration Lewis Research Center Cleveland, Ohio 44135	13. Type of Report and Period Covered: Technical Memorandum

12. Sponsoring Agency Name and Address	14. Sponsoring Agency Code
National Aeronautics and Space Administration Washington, D.C. 20546	

15. Supplementary Notes

Prepared for the Twenty-fourth Aerospace Sciences Meeting sponsored by American Institute of Aeronautics and Astronautics, Reno, Nevada, January 6-9, 1986.

16. Abstract

A rapid quasi-three-dimensional analysis has been developed for blade-to-blade flows in turbomachinery. The analysis solves the unsteady Euler or thin-layer Navier-Stokes equations in a body-fitted coordinate system. It accounts for the effects of rotation, radius change, and stream-surface thickness. The Baldwin-Lomax eddy-viscosity model is used for turbulent flows. The equations are solved using a two-stage Runge-Kutta scheme made efficient by use of vectorization, a variable time-step, and a flux-based multigrid scheme, which are all described. A stability analysis is presented for the two-stage scheme. Results for a flat-plate model problem show the applicability of the method to axial, radial, and rotating geometries. Results for a centrifugal impeller and a radial diffuser show that the quasi-three-dimensional viscous analysis can be a practical design tool.

17. Key Words (Suggested by Author(s))	18. Distribution Statement
Euler equations, Navier-Stokes equations, Multigrid, Inviscid flow, Viscous flow, Turbomachinery	Unclassified - unlimited STAR Category 01

19. Security Classif. (of this report)	20. Security Classif. (of this page)	21. No. of pages	22. Price*
Unclassified	Unclassified		

*For sale by the National Technical Information Service, Springfield, Virginia 22161